A hybrid Lyot coronagraph for the direct imaging and spectroscopy of exoplanet systems: recent results and prospects

John Trauger*[a], Dwight Moody[a], Brian Gordon[a], John Krist[a], Dimitri Mawet[b]
[a] Jet Propulsion Laboratory, California Institute of Technology, 4800 Oak Grove Drive, Pasadena, CA 91109 USA; [b] European Southern Observatory, Alonso de Cordova 3107, Vitacura 7630355, Santiago, Chile

ABSTRACT

We report our best laboratory contrast demonstrations achieved to date. We review the design, fabrication, performance, and future prospects of a hybrid focal plane occulter for exoplanet coronagraphy. Composed of thickness-profiled metallic and dielectric thin films vacuum deposited on a fused silica substrate, the hybrid occulter uses two superimposed thin films for control over both the real and imaginary parts of the complex attenuation pattern. Together with a deformable mirror for adjustment of wavefront phase, the hybrid Lyot coronagraph potentially exceeds billion-to-one contrast over dark fields extending to within angular separations of 3 λ/D from the central star, over spectral bandwidths of 20% or more, and with throughput efficiencies up to 60%.

We report laboratory contrasts of 3×10^{-10} over 2% bandwidths, 6×10^{-10} over 10% bandwidths, and 2×10^{-9} over 20% bandwidths, achieved across high contrast fields extending from an inner working angle of 3 λ/D to a radius of 15 λ/D. Occulter performance is analyzed in light of recent experiments and optical models, and prospects for further improvements are summarized.

The science capabilities of the hybrid Lyot coronagraph are compared with requirements of the ACCESS mission, a representative exoplanet space telescope concept study for the direct imaging and spectroscopy of exoplanet systems. This work has been supported by NASA's Technology Demonstration for Exoplanet Missions (TDEM) program.

Keywords: exoplanet, coronagraph, active optics

1. INTRODUCTION

Our science objective is the direct observation of mature exoplanetary systems, possibly dynamically full, that harbor exoplanets, planetesimals, and dust/debris structures. The architecture of mature exoplanetary systems, such as our own Solar System, as revealed in direct images of planets and debris structures in reflected starlight, are too faint and too close to the parent star to be observed by conventional observatories on the ground or in space.

Direct coronagraphic imaging and spectroscopy at visible (450–900 nm) wavelengths enables a broad science program that includes a census of nearby known radial velocity (RV) planets in orbits beyond ~1AU; a search for mature exoplanet systems beyond the RV survey limits including exoplanets and debris structures as signposts of unseen planets and planetesimals, as well as investigations of circumstellar dust structures in young stellar objects and proto-planetary nebulae as a probe of the life cycle of planetary systems.

In Section 2, we review our goals for advanced coronagraph technology development, as inspired by the New Worlds Technology Program outlined in the 2010 Astronomy decadal report. Section 3 summarizes what is new in the coronagraph occulting mask design. Section 4 covers the physical layout and optical elements for the reported experiments. Section 5 reports the contrast results, together with insights into coronagraph performance gained in these experiments and model simulations. Section 6 outlines the relevance of the reported results to a representative exoplanet mission concept, followed by an overall summary in Section 7.

*john.trauger@jpl.nasa.gov; phone 818-354-9594

2. OBJECTIVES

2.1 Astro2010 challenge: New Worlds Technology Program

The Astro2010 report[1] notes that "One of the fastest-growing and most exciting fields in astrophysics is the study of planets beyond our solar system…" The report proposes a New Worlds Technology Program, recommending that "in the first part of the decade NASA should support competed technology development to advance multiple possible technologies for a next-decade planet imager…" The work reported here, made possible by support from NASA's TDEM program, seeks to advance high-contrast imaging technology towards readiness for an exoplanet mission.

Among the leading architectures for the imaging and spectroscopy of nearby exoplanetary systems is the space coronagraph, which provides in principle very high (10 billion to one) suppression of diffracted and scattered starlight at very small separations (a few tenths of arcseconds) from the star. The concept of a band-limited Lyot coronagraph[2], provides the theoretical basis for mathematically perfect starlight suppression. In practice, the optical characteristics of available materials and practical aspects of the fabrication processes impose limitations on contrast levels and spectral bandwidths that are achievable in the real world. Nevertheless, the band-limited Lyot coronagraph approach has produced the best laboratory-validated performance among all known coronagraph types for contrast, spectral bandwidth, inner working angles, and overall throughput, and alone it has demonstrated high-contrast imaging performance at levels required for exoplanet exploration[3].

Building on the experiences to date with the hybrid Lyot coronagraph concept, we now seek to advance the state-of-the-art by attacking the factors that limit spectrally broadband coronagraph performance.

2.2 What is new: optimized occulter design and fabrication

We expect that a space-based visible-wavelength coronagraph would cover the 500–880 nm spectral range in three discrete bands, such as the standard *V*, *R*, and *I* photometric bands. We report experiments with a new hybrid Lyot focal plane mask for one of the three 20% spectral bands. For a survey of potential Jupiter twins orbiting the nearest 100 AFGK stars, a coronagraphic space telescope must be capable of detecting light reflected by a planet in a surrounding dark field exhibiting a raw contrast that is 10^{-9} fainter than the parent star. For Earth twins, the required raw contrast is an order of magnitude smaller. It is expected that post-processing of coronagraph images will provide detection sensitivities to planets an order of magnitude fainter.

2.3 TDEM demonstrations

TDEM demonstrations are intended document progress in the development of key technologies relevant to a space-based coronagraph mission concept, such as ACCESS[3,4], to detect and characterize exoplanets, thereby to gauge readiness to proceed to Phase A mission development. Protocols for the TDEM investigations are as follows. (1) a demonstration in the High Contrast Imaging Testbed[5] (HCIT) is focused on the validation of one key TDEM technology, rather than the validation of overall performance of the HCIT. (2) Success criteria are defined in terms of statistically significant performance demonstrations of the key technology, ideally with minimal sensitivity to experiment factors beyond the TDEM team's control. And (3) due to oversubscription, the period of performance using the HCIT is strictly limited.

Here the angular separations in the coronagraph image are defined in terms of the central wavelength λ_0 and the diameter D of the pupil-defining element of the coronagraph. The width of the spectral band is defined as the ratio $\delta\lambda/\lambda_0$, where $\delta\lambda$ is the full width at half maximum (FWHM) transmittance of the band-defining optical filter and λ_0 is the central wavelength.

As a representative mission concept, ACCESS forms a high contrast dark field centered on the bright central star. The inner working angle ($3\ \lambda_0/D$) is defined by science requirements, while the outer working angle is defined by the highest spatial frequency controlled by a deformable mirror (up to $24\ \lambda_0/D$ with 48 actuators across the pupil diameter). Optical modeling has shown that it is difficult to control the contrast in the dark field close to the image of the target star. This work addresses the most challenging location in the image plane, the inner working angle at the same angular separation as will be required by ACCESS. Our outer working angle ($15\ \lambda_0/D$) is sufficiently large that the physics of the wavefront control problem can be demonstrated with high expectation of applying the same approach to a larger dark fields at a later date.

The goals of this demonstration are more ambitious than the TPFC Milestones[6,7], with smaller inner working angles and broader bandwidths. Our overall goal is to demonstrate coronagraph contrast better than 1×10^{-9} at angular separations of $3\ \lambda_0/D$ and greater in three separate 20% spectral bands (500-600, 600-720, and 720-880 nm) representative of *VRI*

photometry. The subject of this report is the validation of a new hybrid Lyot focal plane mask with a 3 λ/D inner working angle over a single 20% spectral band.

3. OCCULTER DESIGN

3.1 Design method

Coronagraph focal-plane occulting masks have generally been described in terms of attenuation profiles free of any phase shift. However, phase shifts are expected and observed in physical occulting masks, with significant effects at billion-to-one coronagraph contrast levels in spectrally broad light, as required for the direct imaging and spectroscopy of nearby exoplanet systems.

Consider first a mask design with a single metallic layer. Here the objective is an attenuation profile that matches a prescribed band limited form[2] while accepting without change the consequent phase shifts that are imposed by the Kramers-Kronig relation for real optical materials. In general, such "parasitic" phase shifts violate the criteria for band-limited coronagraph occulters, hence a phase profile that is not band-limited. Further, real materials exhibit significant dispersion in optical properties over spectral bandwidths of interest for exoplanet astronomy.

A specific example is a coronagraph mask composed of a single thin metallic film on glass. We refer to the literature[8] for absorbing materials that closely approximate the criteria for zero wavelength dispersion in a deposited film: $n(\lambda)-1 \propto \lambda$ and $k(\lambda) \propto \lambda$. Nickel is selected, as one of the common metals that offer a favorable relationship between the refractive indices and wavelength[9] thus providing useful and nearly constant ODs across the visible spectrum. In previous work[10], we assumed a central wavelength of 800 nm and a target 10% bandwidth. We note that the central wavelength could have been chosen anywhere in the visible wavelength range.

Now consider providing leverage over the phase-shift profile by adding a non-absorbing dielectric layer to the design. Profiled metal and dielectric layers are superimposed on a glass substrate. The thickness profiles of the films are chosen to produce desired attenuation and phase-shift profiles at the central wavelength, as computed for multilayer thin-film code for metal and dielectric films on a fused silica substrate.

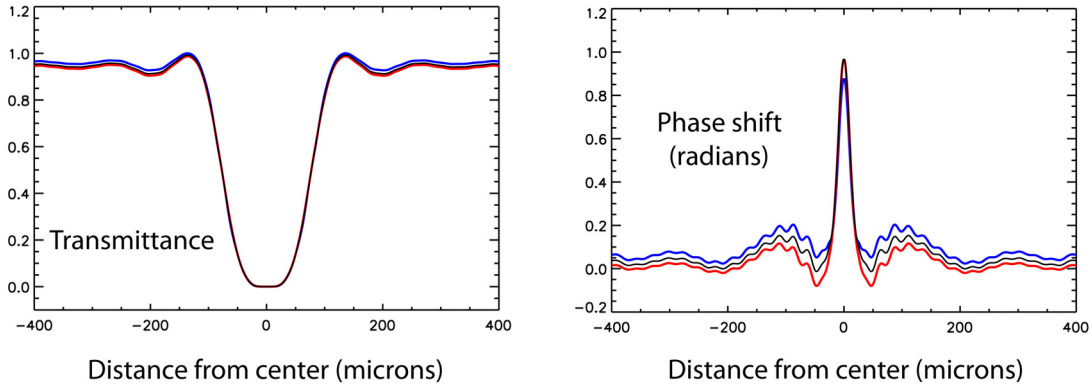

Figure 1. Attenuation and phase shift profiles for the hybrid occulter mask. At left, the attenuation profile reaches 50% transmittance at 3 λ/D from center at the 800 nm central wavelength. At right, the transmitted phase profile. Transmittance and phase profiles are shown at three wavelengths: 720 nm (blue curve), 800 nm (black), and 880 nm (red curve). Physical dimensions are scaled to an f/31.25 beam, for which fλ/D = 25 microns at 800 nm.

For the hybrid design, we begin with a pair of band-limited profiles for the real and imaginary parts of the mask attenuation profile, which is now acknowledged to be complex. The form for the real part of the amplitude profile is a approximately a sinc-squared profile, with the width parameter adjusted to give 50% attenuation at a 3 λ_0/D inner working angle (IWA) from the central "star," in an f/31.25 beam at the 800 nm central wavelength:

$$A_{REAL} = \max(10^{-4}, A_S), \text{ where } A_S(x) = 1 - \left(\frac{\sin(\pi x/w)}{(\pi x/w)} \right)^2$$

In specifying the imaginary part, we again seek a profile that is approximately band limited, as follows:

$$A_{IMAGINARY} = \alpha \left(\frac{\sin(\pi x / w_1 + \pi)}{(\pi x / w_1 + \pi)} \right) + \alpha \left(\frac{\sin(\pi x / w_1 - \pi)}{(\pi x / w_1 - \pi)} \right)$$

where $-0.49 < \alpha < 0.49$ is a design parameter. Next, this complex attenuation profile is decomposed in terms of amplitude and phase:

$$OD_{metal+dielectric}(x) = -2 \log_{10} \left\| A_{REAL} - j A_{IMAGINARY} \right\|$$

$$\delta\, phase_{metal+dielectric}(x) = phase\left(A_{REAL} - j A_{IMAGINARY} \right)$$

The optical characteristics of the hybrid occulting mask is computed using thin film equations and bulk optical indices for the metal and dielectric layers, chosen to be nickel and cryolite. For monochromatic light, this design provides, in principle, essentially perfect attenuation in the dark field, i.e., the predicted contrast is better than 5×10^{-11} everywhere in the dark field beyond 3 λ/D from the star. In this case, the contrast achieved in the laboratory is not limited by the coronagraph design, rather the limits are imposed by other larger sources of background light in the HCIT, amounting to about 1.7×10^{-10} in our best narrowband results, due to scattering from optical imperfections and incoherent stray light.

We expect significant wavelength-dependent variations in the occulter phase shift profiles, hence the best broadband design requires a deviation from the band-limited ideal, and instead we use end-to-end Fresnel propagation code to find an optimal solution specifically for a 20% spectral bandwidth. Using the band limited design above as the starting point in the optimization, we now consider the metal and dielectric profiles as a set of free parameters, along with the phase settings on the DM, and seek a solution simultaneously in the profile parameters and DM settings that gives the best average contrast over the 720-880 nm band. We find that the phase shift profile at distances closer than 2 λ/D have little effect on the overall contrast, hence the design process applies a greater emphasis on phase control outside 2 λ/D. The profiles in Figure 1 reduce phase shifts beyond 2 λ/D while providing nearly zero correction to the central peak phase shift generated by the nickel layer. The predicted contrast for this design is 1.3×10^{-10} over the 20% spectral band (720-800 nm) everywhere in the 3-15 λ_0/D dark field.

3.2 Mask Manufacturing Technique

The OD and phase shift profiles were converted into thickness profiles for the metal and dielectric films. The physical mask was fabricated by vacuum deposition. The design anticipated the effects of the deposition mask, a slit of width 15 microns. The vacuum deposition apparatus is illustrated in Figure 2.

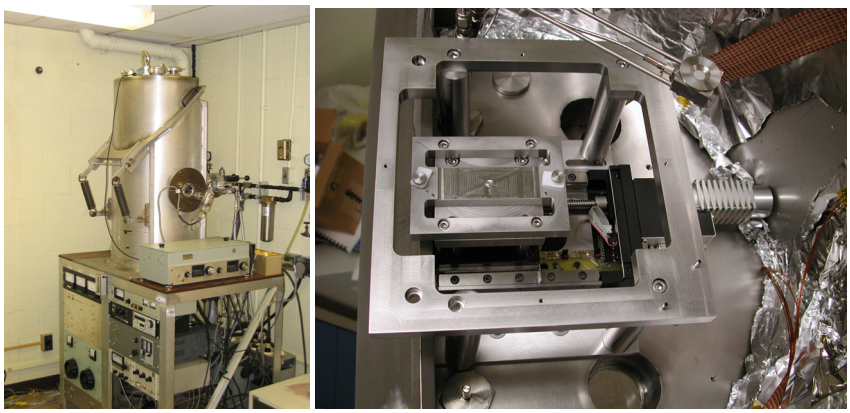

Figure 2. At left, the vacuum deposition plant. At right, the linear motion mechanism used to translate the occulter substrate behind the deposition mask in computer-controlled 1-micron steps. Dwell times are calibrated to produce the desired thickness profiles.

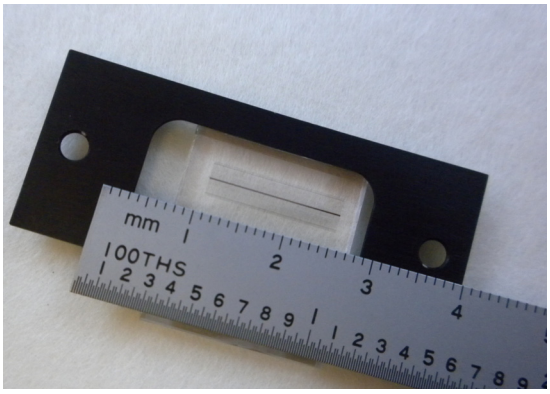

Figure 3. The linear metal-dielectric focal plane mask. The transmittance profile reaches half-transmittance at ±3 λ/D (± 75 microns in an f/31.25 beam at 800 nm) from the line center.

A table of relative dwell times for deposition through the slit at each position across the substrate was generated using a measured relation between OD of the deposited metal film vs. the physical thickness as indicated by a crystal monitor. An anti-reflection coated fused silica substrate was mounted on a translation stage driven in 1-micron steps by a computer-controlled stepper motor. Deposition was carried out over multiple passes of the slit across an overall four millimeter pattern width, while monitoring the accumulated thickness profile. The deposition was terminated when the accumulated thickness at the peak of the profile indicated that the peak OD was within 2% of the target value.

4. LABORATORY EXPERIMENT

4.1 HCIT coronagraph layout

The early demonstrated success of the Lyot coronagraph is due, in part, to its relative simplicity. The achievable contrast, inner working angle, spectral bandwidth, and throughput are all sensitive to surface figure errors and reflectance irregularities on the mirrors, optical misalignments and drift, scattered light from dust and surface defects, stray light, and polarization effects from off-axis mirrors and other components. The Lyot coronagraph design is aided by accurate end-to-end optical propagation models, informed with the representative figure errors in the mirror surfaces, well-characterized deformable mirror influence functions, and high-fidelity descriptions of the key coronagraph elements. The current optical layout of the HCIT Lyot table is shown in the Figure 4. The optical system resides in a vacuum chamber evacuated to ~10 milliTorr levels. The coronagraph is operated remotely, with computers to control source filter selection, shutter, deformable mirror settings, occulter x/y/z location, Lyot stop selection and centering, and CCD camera focal position.

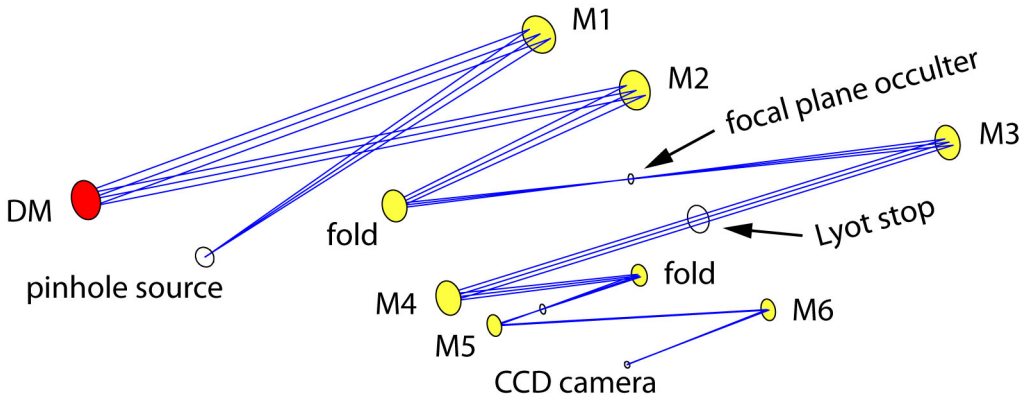

Figure 4. Optical layout of the HCIT Lyot coronagraph table. The optical elements, in the optical path starting from the source, are as follows. The source of continuum light illuminates M1, the first of six off-axis paraboloidal (OAP) mirrors. The beam is collimated by M1, then passes to the deformable mirror (DM) where a

circular stop defines the 48 mm diameter pupil of the system. The DM is from Xinetics, providing a continuous deformable facesheet driven by 2304 actuators within the 48 mm diameter pupil stop. The collimated light is then focused to f/31.25 by M2 and folded by a flat mirror, then passing to the focal plane where the hybrid Lyot occulter is located. The beam is collimated by M3 on its way to the Lyot stop, which is located in a pupil plane conjugate to the deformable mirror. The collimated beam is then brought to a focus by M4 to create the high-contrast coronagraph image. A camera, formed by M5 and M6, then magnifies and projects the coronagraph image onto the CCD focal plane.

4.2 Deformable Mirror

Active control of the optical wavefront is required. Coronagraph elements are designed to suppress the diffracted light common to all telescopes. While ideal coronagraphs perform well in simulations with a mathematically perfect wavefront, it is unrealistic to base the design on ideal theoretical performance alone. Light scattered by mirror surface irregularities establishes a contrast floor that cannot be overcome by coronagraphic techniques. As a rule of thumb, a wavefront corrected at n locations across the aperture diameter (e.g. using a DM that maps $\pi n^2/4$ actuators across the primary mirror) yields a contrast floor $C = \pi(8\sigma)^2/(n\lambda)^2$, where σ is the rms surface error in the DM actuator settings, assumed random and uncorrelated. For example, with $n = 48$ (a total of 1810 actuators within a circular stop), $\sigma = 0.04$ nm rms (or better) is required for the raw instrument contrast $C = 2\times10^{-10}$ observed in these experiments over the 3-15 λ/D dark field in 2% bandwidth light centered at 800 nm.

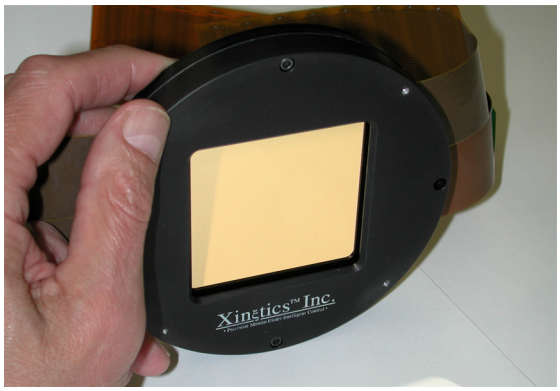

Figure 5. The deformable mirror (DM) used in this laboratory demonstration. The mirror facesheet, made of fused silica, is polished to a nominal surface flatness of λ/100 rms in the unpowered state. The facesheet is driven by a 64×64 mm array of actuators. For these experiments, the DM was stopped down to a diameter of 48 mm (1810 actuators). Control of mirror surface figure, as demonstrated in our experiments, is 0.05 nm rms or better averaged over the 1×1 mm domain of control for each of the 2304 actuators. The DM have been manufactured by Northrop Grumman Xinetics.

Two wavefront sensing and control methods are used. Both methods avoid the complication of non-common-path wavefront errors by using only imagery of a star at the science focal plane. The first is the Gerchberg-Saxton method, used for verification of coronagraph alignment and initial DM settings, which requires as input a set of focus-diversity images of the "star" with the coronagraph elements temporarily removed from the beam. The second is the EFC method[11,12], that uses deterministic settings of the DMs to probe the complex (amplitude and phase) wavefront and iteratively reduce the energy scattered within the coronagraph dark field.

4.3 Supercontinuum light source

The "star" for our experiment is a 5 micron pinhole. Broadband continuum light from a supercontinuum laser, transmitted by single mode fiber to the optical table, is relayed by a pair of lenses to the pinhole. The CCD at the science focal plane receives approximately 10^7 detected photons/nm/second, a flux roughly equivalent to the light collected from a V=1 star by a 1.5 m telescope.

For a space coronagraph, the spectrum of starlight light illuminating the coronagraph would resemble black body radiation. In practice, the spectral distribution produced by the fiber-coupled supercontinuum laser is smooth and continuous across a 20% spectral band, but with brightness that varies significantly with wavelength. A further complication is introduced by the need to couple the supercontinuum radiation into an optical fiber that feeds light to the

coronagraph, where drifts in the alignment between the supercontinuum output fiber and the input fiber leading to the coronagraph can modulate the spectrum of the light reaching the coronagraph. The spectrum of the light source is monitored by periodically by introducing a pinhole and grism into the optical path, in place of the occulter and Lyot stop respectively, then recording the spectrum directly on the science CCD.

As such, a single filter spanning a 20% spectral band would not provide a reliable test of the contrast over the entire spectral band. Instead, the contrast is measured in smaller passbands, either 2% or 7%, that sample the full 20% band. The measurements in each 2% and/or 7% band are individually calibrated against the "star" brightness in that band, then averaged to estimate the contrast metric over the full 20% spectral band. This procedure effectively corrects for any variations in the spectral shape in the supercontinuum spectrum emanating from the source pinhole inside the vacuum chamber.

5. RESULTS AND PROSPECTS

5.1 Results in 2% bandwidth: 2%, 10%, 20%

Contrast demonstrations were carried out during a 12-week run on the HCIT. First experiments sampled the 20% passband in five 2% filters: 720-736, 760-776, 792-808, 824-840, and 864-880 nm. In each iteration of dark field nulling, EFC probing was performed individually in all five filters, then the DM settings were updated with a solution that gave the best contrast averaged over the five bands. As noted in Section 4.2, this procedure leads to a reliable estimate of the average contrast over the overall 20% passband. The nulling was continued, at a cadence of about 4 iterations per hour, until the best contrast was achieved and repeated for many (10-100) iterations. The achieved contrast, measured at an inner 3-4 λ_0/D fiducial box, and averaged over the 3-15 λ_0/D dark field, is listed in Table 1 and illustrated in Figure 6. The experiment was repeated from scratch three times, with the star at different occulter positions, in each case reaching comparable results.

Similarly, demonstrations were carried out over a 10% passband, this time sampling the passband with the following five 2% filters: 760-776, 776-792, 792-808, 808-824, and 824-840 nm. As before, the demonstrations were carried out from scratch three times, with different occulter locations, each time reaching the achieved contrast for many iterations.

Finally, the demonstrations were carried out for a single 792-808 nm filter. The contrast quickly converged on the numbers shown in Table 1 and Figure 6, maintaining a stable contrast value for over 100 successive iterations.

Table 1. Measured contrast, dark field nulling carried out simultaneously with 2% bandwidth filters.

Spectral band	Contrast (3–4 λ_0/D)	Contrast (3–15 λ_0/D)
2.0% (792–808 nm)	3.2×10^{-10}	2.0×10^{-10}
10% (760–840 nm)	6.0×10^{-10}	5.2×10^{-10}
20% (720–880 nm)	2.0×10^{-9}	2.0×10^{-9}

Together, these experiments probe the ultimate contrast limits achievable in the HCIT laboratory. Experiments in a single 2% band (792-808 nm) are sensitive to possible wavefront errors due to DM driver noise, minor chromatic variations in the occulter characteristics over the 2% passband, and incoherent scattered light that manages to rejoin the beam, all of which would limit the effectiveness of the EFC wavefront sensing. In the case of the single 2% passband, wavefront sensing discerns coherence in background light that contributes only 3.5×10^{-11} to the total contrast, while the remaining light, contributing 1.7×10^{-10} to the total contrast, is unresponsive to the EFC probes.

Experiments in 10% and 20% clearly show chromatic variations that are unambiguously attributable to the occulting mask itself. We have investigated the source of these chromatic effects, in terms of laboratory imagery in both the Lyot and focal plane, interpreted by comparisons with our testbed models, and trace them to an error in the calibration of the dielectric deposition process. Future work will correct this unambiguous error in fabrication, and future testbed investigations are expected to confirm a contrast approaching the predicted 1.3×10^{-10} averaged over the 20% passband.

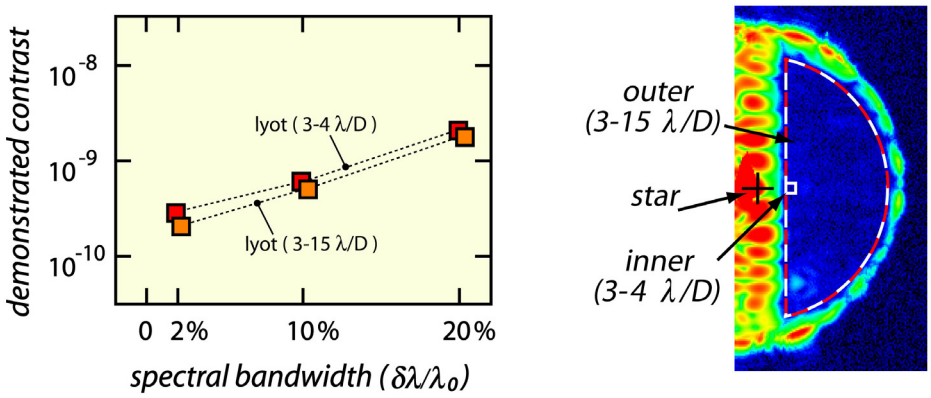

Figure 6. Summary of measured raw contrast for the inner 3-4 λ/D field, and averaged over the 3-15 λ/D outer field, for experiments in spectral bandwidths of 2%, 10%, and 20% as indicated.

5.2 Results of nulling in 7% bandwidth

A second series of experiments was carried out to demonstrate the creation of a dark field in wider passbands, as would be desired in an exoplanet mission scenario where calibration time competes against science observations, placing a premium on wavefront sensing methods that utilize more continuum photons, leading to higher SNRs and quicker solutions. Three 6-7% filters were used: 720-760, 760-833, 833-880 nm. As above, for each iteration of dark field nulling, EFC wavefront sensing was carried out in the three filters individually, then the DM settings were updated with a solution that gave the best contrast averaged over the three bands. Achieved contrast is listed in Table 2.

Table 2. Measured contrast, dark field nulling carried out simultaneously with 6% bandwidth filters.

Spectral band	Contrast (3–4 λ_0/D)	Contrast (3–15 λ_0/D)
6.3% (771–821 nm)	5.6×10^{-10}	5.1×10^{-10}
20% (720–878 nm)	1.8×10^{-9}	1.7×10^{-9}

6. RELEVANT SPACE CORONAGRAPH MISSION CONCEPTS

6.1 Representative concept

ACCESS[3,4] is designed to reveal planets and dust structures by reducing the scattered and diffracted light to within a few hundred milliarcseconds of a star at a level three orders of magnitude lower than any current instrument in space or on the ground, using a stable 1.5 meter diameter telescope, a coronagraphic system for control of diffracted light, active wavefront correction and suppression of scattered light, and a low-noise CCD focal plane and integral field spectrograph viewing the target systems in multiple spectral bands simultaneously.

The ACCESS study compared the performance and readiness of four major coronagraph architectures. ACCESS studied a conceptual space observatory platform as a "level playing field" for a science and engineering evaluation of the coronagraph mission. It included laboratory validation of representative coronagraph types as a second "level playing field" for assessing coronagraph hardware readiness. ACCESS exemplifies a genre of scientifically compelling mission concepts built upon mature subsystem technologies, and evaluates the science reach of a medium-class coronagraph mission.

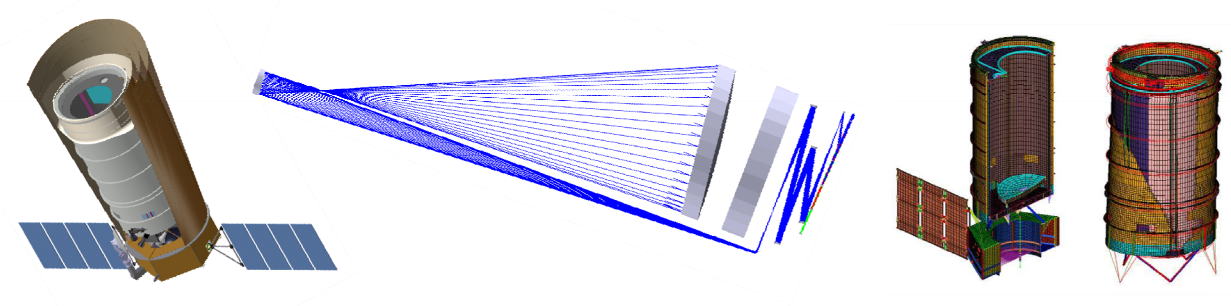

Figure 7. The ACCESS observatory. At left, a rendering of the telescope, spacecraft, multilayer sunshade, and solar panels. At center, a Zemax diagram of the off-axis Gregorian telescope, tracing the rays as they fold into the coronagraph located in the shadow of the primary mirror. At right, extensive thermal and dynamic modeling provides design guidance and reliable predictions of the optical and mechanical stability of the observatory.

The spacecraft provides payload platforms, equipment mounting panels, solar arrays, star trackers, propulsion modules, and thermal control elements. The attitude of the spacecraft is maintained by reaction wheels, using a hierarchy of knowledge from a coarse sun sensor, a pair of star trackers, and pointing knowledge from the coronagraph. A propulsion system is provided for L2 orbit insertion, station keeping, reaction wheel momentum dumping, and attitude control during contingency operations. The temperature of the payload and spacecraft components is maintained by a thermal control subsystem, including a surrounding multilayer sunshade.

6.2 Relevance to mission concept validation

Many aspects of this work are directly applicable to the validation of a space mission concept. The basic coronagraph elements, the focal plane and Lyot masks, are robust and flight-worthy. The deformable mirror technology is currently undergoing a protoflight qualification program. A single Fresnel propagation "computational engine" is used for occulter design, dark field algorithm refinement, real-time testbed nulling control, analysis of testbed components and systems as guidance for the experiment, and is used in conjunction with engineering models of the conceptual observatory for science simulations and performance predictions. Nevertheless, there are several important differences between the lab demonstration and the ACCESS flight implementation. Each is addressed briefly.

A single deformable mirror: The milestone demonstrations will be carried out with a single DM, which allows the control of phase and amplitude in the complex wavefront over one half of the coronagraph field described in Section 5 above. In flight, it is expected that a pair of DMs will be used, in series, to generate a full (two-sided) dark field, with the added advantages of a deeper contrast field and better broadband control.

Starlight: Unlike the light collected by a telescope from a target star, the light intensity on the testbed is not uniform across the pupil. Typically this non-uniformity is a center-to-edge "droop" of a few percent corresponding to the diffraction pattern from the source pinhole. This small amount of non-uniformity has negligible effect on the final contrast if it is accounted for in the wavefront control algorithm, and would result in a finite but negligible loss of contrast if it were ignored in the control algorithm.

Spacecraft dynamics: A control system is required in flight to stabilize the light path against motions of the spacecraft. The dominant effects of spacecraft dynamics are jitter of the star image on the coronagraph focal plane mask and beam walk in the optics upstream of the focal plane mask. For a specific example, the ACCESS analysis showed that for fourth-order coronagraphs with an inner working angle of $3\lambda_0/D$, such as the Lyot coronagraph in this study, pointing errors needed to be less than $\pm 0.03\ \lambda_0/D$ to limit the corresponding contrast degradation to less than 2×10^{-10}. The ACCESS concept model has shown that the required pointing stability can be achieved in space with current high Technology Readiness Level (TRL) systems.

Scaled to the HCIT, this pointing requirement would correspond to an ability to center the occulting mask on the "star" within one micron, or about 0.23 pixels when projected to the CCD focal plane. The milestone demonstration requires the passive stability of the testbed, including the centration of the star on the occulter as one example, which is untraceable to spacecraft dynamics. In practice, during the period of experiments reported here, the HCIT typically exhibited occulter alignment and star positioning drifts of one micron / day or better. As such, the HCIT alignment stability is well within requirements for contrast better than 2×10^{-10}.

7. SUMMARY

In summary, we have reported the best laboratory contrast results to date, with inner working angles of 3 λ/D and bandwidths of 2%, 10, and 20%, demonstrated in the HCIT as part of the TDEM program. Broadband contrast falls a short of model expectations by a factor of a few, and we have traced the shortfall to an error in calibration of the dielectric thickness profile. Future work will correct this fabrication error. These results advance the readiness for a viable space coronagraph mission for the direct imaging and spectroscopy of exoplanetary systems.

ACKNOWLEDGEMENTS

The research described in this paper was carried out at the Jet Propulsion Laboratory, California Institute of Technology, under a contract with the National Aeronautics and Space Administration.

REFERENCES

[1] National Research Council Committee for a Decadal Survey of Astronomy and Astrophysics, [New Worlds, New Horizons in Astronomy and Astrophysics], ISBN 0-309-15800-1 (2010).
[2] Kuchner, M.J., and W.A. Traub, "A Coronagraph with a Band-limited Mask for Finding Terrestrial Planets," Ap.J. 570, 900 (2002).
[3] Trauger, J. *et al*., "ACCESS – A Concept Study for the direct imaging and spectroscopy of exoplanetary systems," *Proc. SPIE* **7731**, 773128, 2010.
[4] Trauger, J. *et al*., "ACCESS – A Concept Study for the Direct Imaging and Spectroscopy of Exoplanetary Systems," *Pathways towards Habitable Planets, ASP Conf. Series* **430**, 375, 2010.
[5] Trauger, J., A. Give'on, B. Gordon, B. Kern, A. Kuhnert, D. Moody, A. Niessner, F. Shi, D. Wilson, and C. Burrows, "Laboratory demonstrations of high-contrast imaging for space coronagraphy," Proc. SPIE 6693, 66930X (2007).
[6] Trauger, J., et al., "TPF-C Milestone #1 Report," JPL Document D-35484 (2006).
[7] Kern, B. et al., "TPF-C Milestone #2 Report," JPL Document D-60951 (2008).
[8] Palik, E., Handbook of Optical Contants of Solids, Academic Press, New York, 1998.
[9] Balasubramanian, K., D. Wilson, B. Kern, E. Sidick, "Thickness-dependent optical properties of metals and alloys applicable to TPF coronagraph image masks", Proc. SPIE 6693, 66930Z, 2007.
[10] Moody, D., B. Gordon, and J. Trauger, "Design and demonstration of hybrid Lyot coronagraph masks for improved spectral bandwidth and throughput," Proc. SPIE 7010, 70103P (2008).
[11] Give'on, A., B. Kern, S. Shaklan, D. Moody, L. Pueyo, "Broadband wavefront correction algorithm for high-contrast imaging systems," Proc. SPIE 6691, 66910A (2007).
[12] Borde, P., and W. Traub, "High-contrast imaging from space: speckle nulling in a low aberration regime," Ap.J. 638, 488 (2006).